The Seasonal Atmospheric Response to Projected Arctic Sea Ice Loss In the Late 21st Century

Clara Deser [1]

Robert Tomas [1]

Michael Alexander [2]

David Lawrence [1]

[1] National Center for Atmospheric Research

[2] NOAA Earth System Research Laboratory

Submitted to the *Journal of Climate*

January 23, 2009

Corresponding author: Dr. Clara Deser, Climate and Global Dynamics Division, NCAR, P.O. Box 3000, Boulder CO 80307 cdeser@ucar.edu

Abstract

The authors investigate the atmospheric response to projected Arctic sea ice loss at the end of the 21st century using an atmospheric general circulation model (GCM) coupled to a land surface model. The response was obtained from two 60-yr integrations, one with a repeating seasonal cycle of specified sea ice conditions for the late 20th century (1980-1999) and one with that of sea ice conditions for the late 21st century (2080-2099). In both integrations, a repeating seasonal cycle of SSTs for 1980-1999 was prescribed to isolate the impact of projected future sea ice loss. Note that greenhouse gas concentrations remained fixed at 1980-1999 levels in both sets of experiments. The 20th and 21st century sea ice (and SST) conditions were obtained from ensemble mean integrations of a coupled GCM under historical forcing and SRES A1B scenario forcing, respectively.

The loss of Arctic sea ice is greatest in summer and fall, yet the response of the net surface energy budget over the Arctic Ocean is largest in winter. Air temperature and precipitation responses also maximize in winter, both over the Arctic Ocean and over the adjacent high latitude continents. Snow depths increase over Siberia and northern Canada due to the enhanced winter precipitation. Atmospheric warming over the high latitude continents is mainly confined to the boundary layer (below ~ 850 hPa) and to regions with a strong low-level temperature inversion. Enhanced warm air advection by sub-monthly transient motions is the primary mechanism for the terrestrial warming. A significant large-scale atmospheric circulation response is found during winter, with a baroclinic (equivalent barotropic) vertical structure over the Arctic in November-December (January-March). This response resembles the negative phase of the North

Atlantic Oscillation in February only. Comparison with the fully coupled model reveals that Arctic sea ice loss accounts for most of the seasonal, spatial, and vertical structure of the high latitude warming response to greenhouse gas forcing at the end of the 21st century.

1. Introduction

Arctic sea ice extent has declined over the past several decades, with the largest rate of retreat (~ -10% per decade) in late summer (Serreze et al., 2007; Comiso et al., 2008; Deser and Teng, 2008; among others). The rate of decline has accelerated substantially in the past decade, and now outpaces that simulated by most climate models in response to increasing greenhouse gas (GHG) concentrations (Stroeve et al., 2007). The record losses of perennial Arctic sea ice in both 2007 and 2008 highlight the ongoing trajectory towards ice-free summers, a state which climate models project may be realized within 15-50 yrs (Holland et al., 2006).

A seasonally ice-free Arctic Ocean is expected to have widespread socio-economic, ecological and climatic consequences. For example, commercial shipping routes and energy resource development in the Arctic are likely to change, impacting native populations and habitat. Warming associated with Arctic sea ice loss may hasten permafrost degradation (Lawrence et al., 2008) and lead to trophic mismatch (Post and Forchhammer, 2008). Atmospheric circulation patterns and accompanying precipitation and storm track distributions over middle and high latitudes may also be affected (Sewall, 2005; Singarayer et al., 2006; Gerdes, 2006; Seierstad and Bader, 2008).

Identification of the climatic impacts of a seasonally ice-free Arctic Ocean from observational data alone is difficult due a variety of factors, including: 1) that the loss of perennial Arctic sea ice is not yet complete; 2) the confounding presence of climate variability due to internal atmospheric processes and/or forced by factors other than Arctic sea ice loss; and 3) that observational data contain a mixture of forcing and response. To circumvent these difficulties, we use an atmospheric modeling approach to

address the atmospheric response to projected future Arctic sea ice loss. The model results may be useful for informing observational attribution studies of the climatic effects of Arctic sea ice retreat. For example, is the enhanced Arctic warming in autumn over the past few years an early signal of the emerging climate response to Arctic sea ice loss as proposed by Serreze et al. (2008)?

Many studies have used atmospheric general circulation models to investigate the effects of prescribed changes in Arctic sea ice cover upon the atmosphere. The specified sea ice extent or concentration conditions range from realistic values for winter (Alexander et al., 2004; Singarayer et al., 2006) and summer (Bhatt et al., 2008) to more idealized configurations (realistic spatial patterns with exaggerated amplitudes) within the Atlantic (Magnusdottir et al., 2004; Deser et al., 2004; Kvamsto et al., 2004) and Pacific (Honda et al., 1999) sectors in winter. Focusing on dynamical aspects, these studies reported a range of atmospheric circulation responses depending on the location and polarity of the sea ice changes as well as time of year. For the Atlantic sea ice cases, the winter circulation response was found to resemble the North Atlantic Oscillation (NAO; Hurrell, 1995) or Northern Annular Mode (NAM; Wallace, 2000), the leading structure of internal atmospheric variability over the extratropical northern hemisphere. For the Pacific sea ice case, the winter circulation response consisted of a stationary Rossby wavetrain downstream of the Sea of Okhotsk and extending across the Pacific into North America. The summer circulation response to sea ice changes within the Arctic Ocean displayed a significant remote effect over the north Pacific.

In addition to 'present-day' sea ice conditions, projected future changes in Arctic sea ice concentrations at the end of the 21st century have been prescribed as boundary

conditions to atmospheric general circulation models. Singarayer et al. (2006) employed idealized scenarios of future Arctic sea ice loss, while Seierstad and Bader (2008) used Arctic sea ice loss projections taken from coupled model simulations driven by increasing greenhouse gas (GHG) concentrations. The former study focused upon the wintertime (December-February average) responses in circulation, precipitation and surface air temperature; while the latter was concerned mainly with the circulation response, contrasting December-February and March. Singarayer et al. (2006) reported reductions in sea level pressure over the Arctic, northeastern Canada and the Bering Sea, accompanied by local increases in precipitation and air temperature. Seierstad and Bader (2008) showed a positive 500 hPa geopotential height response over the Atlantic sector of the Arctic in December-February, and an amplified circulation response in March that resembles the negative polarity of the NAO/NAM. Due to a lack of information on the vertical structure of the circulation responses in the two studies, it is difficult to make a direct comparison between them.

The present study aims to provide a more comprehensive assessment of the atmospheric response to projected Arctic sea ice loss at the end of the 21st century than earlier studies, including aspects not previously addressed in detail such as seasonal dependence and vertical structure. For example, we document the full seasonal cycle of the three-dimensional circulation response to future Arctic sea ice loss. Another focus of our study is the terrestrial climate response to future Arctic sea ice loss, including effects on air temperature, precipitation and snow depth. We also investigate the role of atmospheric boundary layer stability in determining the geographical distribution and vertical structure of the terrestrial climate response. In addition to terrestrial impacts, the

seasonal cycle of the response of the Arctic Ocean surface energy balance is investigated. Finally, we compare the atmospheric response to future Arctic sea ice loss with the atmospheric response to GHG forcing in a fully coupled climate model in order to assess the relative role of Arctic sea ice loss in future climate change. Early results on the terrestrial air temperature response were presented in Lawrence et al. (2008).

We note that our atmospheric modeling approach is designed to isolate the direct impact of future sea ice loss upon the atmosphere, without accounting for feedbacks from the oceans or other components of the climate system. As such, it may be used as a baseline for evaluating the impact of Arctic sea ice loss upon the atmosphere.

The paper is organized as follows. The model and experimental design are described in Section 2. Results are presented in Section 3. Summary and discussion are given in Sections 4 and 5, respectively.

2. Model experiments

To address the impacts of projected future changes in Arctic sea ice cover upon the global atmospheric circulation and climate, we have conducted two experiments with the Community Atmospheric Model Version 3 (CAM3), an atmospheric general circulation model with a horizontal resolution of ~ 1.4º latitude and 1.4º longitude (T85) and 26 vertical levels, coupled to the Community Land Model (CLM). The model's physical and numerical methods are documented in Collins et al. (2006) and references therein. Aspects of the model's mean state are described in Hurrell et al. (2006) and Hack et al. (2006).

The CAM3 'control' experiment consists of a 60-year integration with a specified repeating seasonal cycle of SSTs and sea ice (concentration and thickness) for the period 1980-1999, obtained from the 7-member ensemble mean of 20th century Community Climate System Model Version 3 (CCSM3) simulations at T85 resolution. CCSM3 is a fully coupled climate model comprised of CAM3, CLM, the Parallel Ocean Program model, and the Community Sea Ice Model version 4. The CCSM3 20th century simulations are forced with observed estimates of time-varying atmospheric chemical composition (greenhouse gases, tropospheric and stratospheric ozone, and sulfate and volcanic aerosols) and solar output as described in Meehl et al. (2006), and are conducted without flux adjustments.

The CAM3 'perturbation' experiment consists of a 60-year integration with a repeating seasonal cycle of Arctic sea ice (concentration and thickness) for the period 2080-2099, taken from the 8-member ensemble mean of 21st century CCSM3 simulations at T85 resolution under the SRES A1B greenhouse gas forcing scenario. For the CAM3 experiments with prescribed sea ice conditions for the late 21st century, SSTs are set to those in the control experiment so as to isolate the impact of the sea ice changes. At grid boxes where fractional sea ice cover in the late 20th century is replaced by open water in the late 21st century, SSTs are set to the freezing point of sea water (~ -1.8°C). A two-sided Student's t-test is used to evaluate the statistical significance of the atmospheric changes between the 60-yr averages of the control and perturbation experiments.

Our experimental design is similar to the studies of Singarayer et al. (2006) and Seierstad and Bader (2008) except: 1) we do not include any changes in SSTs; 2) we

include sea ice thickness as well as concentration changes; and 3) our ensemble size is considerably larger and the horizontal resolution of our atmospheric GCM is doubled.

3. Results

a. Arctic sea ice concentration and thickness

The prescribed sea ice concentration (SIC) and sea ice thickness (SIT) distributions for the late 20th century (1980-1999) and late 21st century (2080-2099) CAM3 experiments, taken from CCSM3, are shown in Fig. 1 as bi-monthly averages (January-February, March-April, May-June, July-August, September-October, and November-December). The most dramatic loss of Arctic sea ice between the late 20th and 21st centuries occurs during summer, with a nearly ice-free Arctic Ocean projected during August-October. Although largest in summer, the loss of sea ice occurs year-round as the ice edge retreats from the peripheral Arctic Seas. The areal reduction in Arctic sea ice is accompanied by a thinning of the ice pack. SIT in the central Arctic Ocean decreases from 3-4m to 0.5-1m in winter and from 2.5-3.5m to < 0.5m in summer. The late 20th century SIC and SIT distributions are generally realistic compared to the available observations (Holland et al., 2006).

The bi-monthly changes in SIT and SIC between the late 20th and 21st centuries are shown in the top two rows of Fig. 2. The magnitude and pattern of sea ice thinning is relatively uniform throughout the year, with maximum values ~ 2.5 - 3.5m in the central Arctic Ocean. In contrast, the reductions in SIC are seasonally-dependent, with the largest decreases (~ 80-90%) within the central Arctic Ocean in summer (September-October), and smaller decreases (~ 50-60%) within the marginal seas in winter.

b. Surface energy flux response

The changes in Arctic sea ice are communicated to the atmosphere via changes in the net surface energy fluxes. Figure 2 shows bi-monthly differences between the late 20th and 21st centuries in the surface turbulent energy fluxes (sensible plus latent) and the longwave and shortwave radiative fluxes. The turbulent energy flux response is considerably greater than, and exhibits a different seasonal dependence from, the radiative flux response. The former is largest (maximum amplitudes ~ 60-90 Wm-2) in winter whereas the latter is largest (maximum amplitudes ~ 10-20 Wm-2) in summer (shortwave) and late fall (longwave). The winter maximum of the turbulent energy flux response is due to the fact that this is the time of year when the air temperatures are coolest relative to the underlying surface (ice or open water).

The radiative flux responses (upward for longwave and downward for shortwave) are localized to the SIC changes, whereas the turbulent flux responses exhibit a dipole structure with upward anomalies over the SIC losses and downward anomalies directly to the south (Fig. 2). The downward turbulent heat flux response directly to the south of the SIC changes arises because the region of maximum turbulent heat loss from the ocean to the atmosphere is always located at the ice edge, so when the ice edge moves poleward, a region of diminished upward heat flux is left behind (Deser et al., 2000; Magnusdottir et al., 2004; and Alexander et al., 2004). In reality, the ocean would respond to the heat flux anomalies, resulting in increased SSTs (and reduced downward heat fluxes) in these regions.

A more detailed view of the seasonal cycle of the SIC changes and the surface energy flux response over the Arctic Ocean is given in Fig. 3. For each month, the data were area-averaged over all grid points for which SIC during 1980-1999 exceeds 50%. This criterion encompasses the full region of SIC losses while excluding most of the negative turbulent energy flux response along the equatorward margins of the ice edge. Consistent with Fig. 2, the largest SIC loss occurs in July-November (peaking in October) while the greatest net surface energy flux response occurs in October-February (peaking in November). The delay in the surface energy flux response relative to the maximum SIC loss has important implications for the timing of the atmospheric circulation and climate response.

Indeed, the seasonal cycles of the surface air temperature and precipitation responses over the Arctic Ocean and over the high latitude continents (65º - 80ºN) are in phase with the seasonal cycle of the net surface energy flux response, not SIC (Figs. 4 a and b). (Note that in Figs. 4 and b, the shortwave radiative component is omitted from the net surface energy flux response in view of the fact that the enhanced downward shortwave radiation resulting from the reduced albedo associated with an ice-free Arctic Ocean does not warm the atmosphere directly, but instead warms the ocean, an effect that has been suppressed in our experiments.) Over the Arctic Ocean, the maximum responses occur in November, with values of 17ºC, 0.4 mm d-1, and 67 Wm-2 for temperature, precipitation, and net surface energy flux, respectively (Fig. 4a). Over land, the maximum temperature and precipitation responses occur in November-December, with values of 7ºC and 0.16 mm d-1, respectively (Fig. 4b). The close agreement among the seasonal cycles of the temperature, precipitation and net surface energy flux responses indicate

that the Arctic Ocean net surface energy flux response to sea ice loss exerts a strong local control on climate within the Arctic Ocean (Fig. 4a) and even an important remote control on climate over the adjacent continents (Fig. 4b).

c. Atmospheric temperature response

The bi-monthly net surface energy flux (turbulent plus longwave radiation) response, and the terrestrial air temperature, snow depth and precipitation responses are shown in Fig. 5. Air temperature responses that exceed ~ 0.5ºC (first level of shading) and snow depth responses that exceed ~ 0.75 cm liquid water equivalent in absolute value (second level of shading) are statistically significant at the 5% confidence level based on a two-sided Student's t-test. Precipitation responses significant at the 5% confidence level are outlined with thick black contours in the figure.

Consistent with Fig. 4b, the seasonal cycle of the terrestrial air temperature response follows that of the net surface energy flux response, with maximum warming in winter (November-December and January-February) and weaker warming in autumn (September-October) and spring (March-April). The terrestrial warming is largest in coastal regions adjacent to the Arctic Ocean, with the maximum temperature response over Siberia and northern Canada and Alaska, and penetrates approximately 1500 km inland.

The terrestrial surface air temperature responses in early (November-December) and mid (January-February) winter are largely confined to regions with a mean boundary layer temperature inversion in the late 20th century (marked by thick black contours on the bi-monthly air temperature responses in Fig. 5; note that there is no inversion in the

warm season May-June through September-October). Indeed, the vertical structures of the December atmospheric temperature responses over the Arctic Ocean and high latitude (65º - 80ºN) continents are confined to below ~ 800 hPa, with the warming amplifying towards the surface (maximum values of 6.5 ºC over land and 16 ºC over the ocean; Fig. 6). As a consequence of the vertical structure of the warming, the static stability of the boundary layer decreases from the late 20th century to the late 21st century. Over the ocean, the 10 ºC inversion between 1000 hPa and 900 hPa in the late 20th century is completely eroded in the late 21st century; over land, the capping inversion while not completely gone in the 21st century is only approximately 50% of that in the 20th century (Fig. 6).

The geographical distributions of the strength of the December low-level inversion in the late 20th and 21st centuries are shown in Fig. 7. The marine inversion, which exceeds 12ºC over the central Arctic Ocean in the late 20th century, disappears entirely in the late 21st century. The terrestrial inversion weakens and retreats from far eastern Siberia and the north slope of Alaska in the late 21st century compared to the late 20th century. The inversion strength over the Canadian Archipelago decreases from ~ 14ºC in the late 20th century to ~ 6ºC in the late 21st century.

The seasonal cycles of the strength of the boundary layer temperature inversion over the Arctic Ocean and high latitude continents during the late 20th and 21st centuries are shown in Fig. 8. As before, the Arctic Ocean region is defined on a monthly basis as the area with SIC > 50% during 1980-1999, and the terrestrial region is defined as 65º - 80ºN, 60º - 300ºE. In the late 20th century, the Arctic marine (terrestrial) inversion exists from October through April (November through March), with maximum values ~ 9 ºC in

January. The wintertime Arctic marine inversion almost disappears entirely in the late 21st century, with only a weak vestige left in February-March (1-2 ºC). The wintertime terrestrial inversion also diminishes in strength (maximum values ~ 5 ºC) in the late 21st century, but not as dramatically as the marine inversion, and its onset is delayed to December. The largest changes in inversion strength between the 20th and 21st centuries occur in November-December, with maximum values of ~5 ºC over land and ~15 ºC over the Arctic Ocean (Fig. 8, lower panel).

d. Terrestrial snow cover and precipitation responses

Despite the warming of the atmospheric boundary layer, winter snow depth increases over Siberia, northern Canada and the northern slope of Alaska (Fig. 5). At the end of winter (March-April), snow depth has increased by ~ 1.5 - 3 cm liquid water equivalent over Siberia and ~ 1.0 - 1.5 cm liquid water equivalent over northern Canada and Alaska. Smaller decreases in snow depth occur to the south, primarily over western Russia and the Canadian Rockies. The patterns of snow depth change persist throughout the winter season, emerging in November-December and reaching their maximum amplitude in March-April.

Given the widespread terrestrial warming during the winter season, the increases in snow depth must be a result of enhanced precipitation. Indeed, precipitation increases in early winter (November-December) over Siberia, eastern Alaska and northern Canada, and through mid-winter (January-February) over Siberia (Fig. 5). Several factors may contribute to the precipitation increases, including enhanced water vapor content in the terrestrial boundary layer (due to increased moisture transport out of the Arctic by the

sub-monthly transients; not shown), destabilization of the terrestrial boundary layer due to surface-intensified warming (recall Figs. 6-8), and enhanced low-level convergence associated with decreases in sea level pressure (discussed in Section 3f).

The role of precipitation in the snow depth response is further assessed by comparing the accumulated precipitation during the cold season (October – March) with March snow depth (Fig. 9). The spatial patterns of the two fields are similar, with areas of positive (negative) accumulated precipitation changes generally corresponding to regions of positive (negative) snow depth changes. There is also quantitative agreement between the magnitudes of the positive accumulated precipitation and snow depth responses. Note that the region of positive accumulated precipitation values over Western Europe (excluding Scandinavia) does not correspond to increased snow depth because the air temperature is above 0°C (thick gray curve in Fig. 9, right).

More detail on the seasonal timing of the precipitation, accumulated precipitation, and snow depth responses over Siberia and northern Canada is provided in Fig. 10. The regions are defined using those grid boxes for which the snow depth response in March exceeds 2.5 cm liquid water equivalent. Over northern Canada (Fig. 10a), positive precipitation values occur from October through February, with the largest increases in November-December. The resulting accumulated precipitation response tracks the snow depth response, with a gradual increase throughout the winter to maximum values in February. Similar results are found for Siberia, although there the maximum precipitation increases occur in December-January and the maximum accumulated precipitation and snow depth responses occur in March (Fig. 10b).

e. Heat budget

What processes account for the winter (October-April) air temperature increases over the Arctic Ocean and adjacent continents? We evaluated the terms in the thermodynamic energy equation (e.g., Holton, 1979) using daily model output. The resulting area-averaged heat budget response for the Arctic Ocean (defined as the region with SIC > 50% during 1980-99) is shown in Fig. 11 (left panel). The near-surface warming (1000-950 hPa) is primarily due to vertical diffusion (acting to transmit the upward sensible and latent surface heat flux anomalies; green curve) while the warming in the upper part of the boundary layer (900-850 hPa) is attributable to condensational heating (dashed purple curve; Fig. 11, left). Horizontal temperature advection by both the monthly mean and sub-monthly transient circulation (dashed black and solid black curves) and longwave radiation (solid purple curve) act to cool the boundary layer (Fig. 11, left). Contributions to the heat budget by shortwave radiation and monthly mean temperature tendency are negligible (not shown). The residual term (e.g., the sum of all the terms in the heat budget, including shortwave radiation and temperature tendency) is small compared to the dominant terms in the balance (orange curve in Fig. 11, left panel).

A different balance of terms obtains for the adjacent continents (Fig. 11, right). The high latitude (poleward of 65 ºN) terrestrial boundary layer is warmed by means of horizontal temperature advection by sub-monthly transient atmospheric motions (primarily their meridional component), condensational heating (except at 1000 hPa), and sub-grid scale horizontal and vertical diffusion. Of these, sub-monthly transient advection is the dominant mechanism for warming the lower portion of the boundary layer (below 900 hPa; maximum value ~ 0.80 ºC d-1) while condensational heating

makes a substantial contribution in the upper portion of the boundary layer (but cools the surface). The other terms in the heat budget act to cool the boundary layer, primarily horizontal temperature advection by the monthly mean atmospheric circulation and longwave radiation (shortwave radiation and the monthly mean temperature tendency terms are near zero; not shown). There is also a substantial residual in the heat budget that acts to cool the air at 950 hPa and 1000 hPa; the origin of this residual is not known.

In summary, heat released from the Arctic Ocean under reduced sea ice conditions (primarily via turbulent sensible and latent heat fluxes) is communicated to the Arctic atmospheric boundary layer by vertical diffusion and to a lesser extent condensational heating. The resulting temperature increase is mixed out over the adjacent continents by sub-monthly transient atmospheric motions, causing a warming of the terrestrial atmospheric boundary layer. A similar picture holds for the moisture budget (not shown).

f. Atmospheric circulation response

Unlike the thermodynamic responses discussed above, the dynamical atmospheric response varies greatly from month to month as shown in Fig. 12 for geopotential heights at 1000 hPa and 500 hPa (shading indicates values that exceed the 5% confidence level based on a two-sided Student's t-test). The circulation responses are weak (generally < 10 m and not statistically significant) during the warm season (June – September), in accord with the small response of the net surface energy fluxes. Although the monthly geopotential height responses are larger and statistically significant during the cold season (October – May), they exhibit considerable variation in pattern and amplitude.

The responses in November, December and April exhibit many similarities, including a baroclinic response over the Arctic consisting of negative values (-20 to -30m) at 1000 hPa and positive (10-20m) values at 500 hPa (weak negative values in April), and an equivalent barotropic (e.g., amplifying with height) ridge (trough) response over central and eastern Russia (Bering Sea). A different circulation response is seen in mid-winter, with some degree of consistency among the individual January, February and March patterns. For example, the Arctic is dominated by an upper-level ridge (largest amplitude in January and February ~ 40 - 60 m at 500hPa) accompanied by a negligible response at the surface. Also common to the circulation responses in the mid-winter months is an equivalent barotropic trough over the northeast Pacific and a baroclinic surface trough over the Sea of Okhotsk. In February, the response pattern resembles the negative polarity of the North Atlantic Oscillation (NAO; Hurrell, 1995).

More detail on the vertical structure of the circulation response is given in Fig. 13 which shows transects of the temperature and geopotential height responses along 90º E in early (November-December), middle (January-February) and late (April) winter. In early winter, a shallow baroclinic geopotential height response with a nodal point near 925 hPa develops over the Arctic in association with the ice-induced near-surface warming. Farther south, the response consists of an equivalent barotropic ridge with maximum values ~ 40 m at 250 hPa near 65º N. The Arctic baroclinic response is also evident in mid-winter, but it competes with the equivalent barotropic ridge aloft which weakens the surface trough compared to that in early winter. The late winter response resembles that in early winter, although the Arctic surface trough is less pronounced due to reduced boundary layer warming and there are no positive geopotential height

anomalies aloft. The shallow baroclinic response over the Arctic is consistent with a linear response to enhanced boundary layer heating associated with reduced sea ice, while the equivalent barotropic response to the south (and the equivalent barotropic component of the response over the Arctic in mid-winter) is consistent with a non-linear response involving transient eddy momentum fluxes (e.g., Lau and Holopainen, 1984; Peng et al., 1997; Deser et al., 2007). A quantitative analysis of the momentum balances for each of the monthly circulation responses is beyond the scope of this paper.

Internal modes of circulation variability have been shown to play an important role in shaping the structure of the atmospheric response to external forcing [e.g., anomalous SSTs or sea ice (Peng et al., 1997; Deser et al., 2004) and orbital changes (Hall et al., 2001)]. However, we find little correspondence between the dominant patterns of internal variability (not shown) and the patterns of geopotential height response to Arctic sea ice loss except in February.

There is a weak (20 m) but statistically significant equivalent barotropic trough response localized over the Kara Sea and northern Russia in June and July. The trough response is accompanied by increased precipitation (and decreased precipitation farther south; recall Fig. 5). The dynamical origin of this trough response is unclear.

g. Comparison with CCSM3

How much of the projected northern hemisphere climate response in the fully coupled climate model CCSM3 at the end of the 21st century is due to Arctic sea ice loss? To address this question, we compare the climate response to Arctic sea ice loss in the CAM3 experiments with the climate response to GHG forcing under the SRES A1B

scenario in CCSM3. Figure 14a (top row) shows the CCSM3 bi-monthly terrestrial air temperature response, formed by subtracting the period 1980-1999 taken from the 20th century ensemble mean from the period 2080-2099 taken from the 21st century ensemble mean. The CCSM3 terrestrial air temperature response exhibits the expected poleward amplification in winter, with maximum values exceeding 10 ºC over Siberia and northern Canada in November-December. Weaker and more spatially uniform warming occurs in summer, with values ~ 2 - 5 ºC. Removing the sea ice – induced component from the CCSM3 response (e.g., subtracting the CAM3 response from the full CCSM3 response) eliminates most of the poleward amplification, resulting in a more spatially homogeneous pattern of winter warming over the continents. Indeed, the main structure in the pattern of residual winter air temperature response is zonal rather than meridional, with ~ 2º-4 ºC less warming on the western side of Eurasia relative to the eastern side. This effect, which is most pronounced in early winter (November-December), may be due to advection of maritime air over Europe.

In addition to reducing the spatial inhomogeneity, removing the effect of Arctic sea ice loss also reduces the amplitude of the seasonal cycle of the terrestrial air temperature response in CCSM3. This aspect is documented further in Fig. 14b which shows the seasonal cycles of the CCSM3, CAM3, and sea-ice residual CCSM3 terrestrial air temperature responses averaged over the region 60º - 300ºE poleward of 65ºN. The seasonal marches of the temperature responses are remarkably similar in CCSM3 and CAM3, with maximum warming in November-December (10ºC in CCSM3 and 7ºC in CAM3) and minimum warming in May-August (3º-4ºC in CCSM3 and 0º-0.5ºC in CAM3). The similarity of the amplitude and timing of the seasonal cycles in CCSM3 and

CAM3 results in a relatively constant offset (2º-4ºC) between the two. That is, the sea ice-residual component of the high latitude terrestrial warming in CCSM3 is much less seasonally dependent than the full response, with maximum values ~ 3º-4ºC during July-February and minimum values ~ 2ºC in April-May.

Finally, the vertical structures of the high latitude terrestrial air temperature responses in December for CCSM3 and CAM3 are compared in Fig. 14c. The CCSM3 profile is very similar to CAM3 except for a nearly constant offset of approximately 3ºC. Thus, most of the enhanced warming within the boundary layer (~ 6ºC temperature increase at 1000 hPa relative to that at 800 hPa) results directly from Arctic sea ice loss. The height-invariant sea-ice residual warming in CCSM3 is presumably due mainly to enhanced longwave radiation from increased GHG and water vapor concentrations; advection from lower latitudes may also play a role.

Figure 15 shows the accumulated cold season (October – March) precipitation and March snow depth responses in CCSM3. These may be compared with the CAM3 responses to Arctic sea ice loss shown in Fig. 9 (note the doubled range of the color bar scale in Fig. 15 compared to Fig. 9). The patterns of snow depth response in CCSM3 and CAM3 are similar, but the amplitudes are considerably greater in the coupled model compared to the atmospheric model. In particular, the negative (positive) snow depth response values are 4-5 (1.5-2) times larger in CCSM3 than in CAM3. Warmer air temperatures in CCSM3 relative to CAM3 account for the larger snow reductions, while higher accumulated winter precipitation amounts (associated with the warmer air temperatures) account for the greater snow increases. Both CCSM3 and CAM3 exhibit positive snow depth responses over eastern Russia and northern Canada where the

accumulated precipitation responses are positive and surface air temperatures during 2080-2099 are < -10ºC (thick black contour on snow cover panel in Fig. 15). However, the conditions leading to negative snow depth responses over western Russia, Scandinavia and the southern portion of northern North America differ between the two models: in the case of CCSM3, warmer air temperatures control the decreases in snow depth despite the enhanced winter precipitation; whereas in CAM3, warmer temperatures and decreased precipitation lead to diminished snow cover.

The monthly SLP responses for CCSM3 and CAM3 are compared in Fig. 16. Perhaps the most striking aspect of this comparison is that CCSM3 exhibits a substantial SLP response in the summer months (July-October) that is entirely absent from CAM3. This summer response is quasi-annular in its spatial pattern, with a trough over the Arctic and a ridge over the north Pacific and Atlantic, and exhibits an equivalent barotropic vertical structure (not shown). This comparison indicates that Arctic sea ice loss does not directly drive the high latitude northern hemisphere circulation response in the fully coupled model in summer. There is some similarity between the CAM3 and CCSM3 SLP responses in November, December, January, and May: in particular, both exhibit an Arctic trough in November-December and a lack thereof in January.

4. Summary

We have documented the response of CAM3/CLM3, an atmospheric general circulation model coupled to a land surface model, to projected Arctic sea ice loss at the end of the 21st century. The response was obtained from two 60-yr integrations of the model, one with a repeating seasonal cycle of specified sea ice concentration and

thickness conditions for the late 20th century (1980-1999) and one with sea ice conditions for the late 21st century (2080-2099). In both integrations, the same repeating seasonal cycle of SSTs for the late 20th century (1980-1999) was specified in order to isolate the direct impact of projected future sea ice loss. Note that greenhouse gas concentrations remained fixed at 1980-1999 levels in both sets of experiments. The 20th and 21st century sea ice (and SST) conditions were obtained from ensemble mean integrations of the fully coupled climate model CCSM3 under historical forcing and SRES A1B scenario forcing, respectively.

An important finding of this study is the delayed response of the net surface energy budget over the Arctic Ocean to sea ice loss. Specifically, the loss of Arctic sea ice is greatest in summer and autumn (July-November, peaking in October) yet the response of the net surface energy flux is largest in winter (October-February, peaking in November). This is due to that the turbulent (sensible and latent) energy loss, the dominant term in the net surface energy budget, is greatest when the air temperatures are coolest relative to the underlying surface (ice or open water). The delay in the surface energy flux response relative to the maximum sea ice loss has important implications for the timing of the atmospheric response since the energy fluxes communicate the sea ice change to the atmosphere. Indeed, the seasonal cycle of the climate response to future Arctic sea ice loss was shown to follow that of the net surface energy flux rather than that of the sea ice (e.g., the response is greatest in October-February).

Another important finding is the impact of future Arctic sea ice loss on high latitude terrestrial air temperatures, precipitation, and snow cover. The air temperature and precipitation responses are greatest in November-December over Siberia and

northern Canada, with values ~ 7ºC and ~ 0.16 mm day-1, respectively. As a result of enhanced winter precipitation (and despite the warmer air temperatures), snow depths over Siberia and northern Canada increase by ~ 1 cm liquid water equivalent in late winter (February-April). The climatological air temperature inversion over the high latitude continents in winter plays an important role in determining the geographical distribution and vertical structure of the air temperature response to Arctic sea ice loss. Specifically, the spatial extent of the winter air temperature response is confined to the region with a present-day inversion, and the vertical extent of the temperature response is confined to the boundary layer (e.g., below ~ 850 hPa and amplifying towards the surface). As a consequence of the vertical structure of the terrestrial air temperature response, the static stability of the boundary layer decreases by ~50% from the late 20th century to the late 21st century.

The dominant process warming the atmospheric boundary layer over the high latitude continents is horizontal heat advection by sub-monthly transient atmospheric motions. In other words, high frequency wind fluctuations mix the air warmed over the Arctic Ocean due to enhanced sensible heat loss associated with reduced sea ice cover out over the high latitude continents. Temperature advection by the monthly mean atmospheric circulation acts as a negative feedback, as do all of the other terms in the heat budget except for latent heat release during condensation (e.g., enhanced cloud formation). Similar results are found for the high latitude terrestrial moisture budget.

The seasonal response of the atmospheric circulation to Arctic sea ice loss is also approximately in phase with the timing of the net surface energy flux response. In particular, significant circulation responses are found only during the cold season

(October-April) with insignificant responses during summer. Within the cold season, the spatial and vertical structures of the response differ from month to month. In early winter (November-December), the response is baroclinic over the Arctic, with low pressure anomalies near the surface (maximum values ~ 3-5 hPa) and high pressure anomalies aloft. The baroclinic response over the Arctic is also evident in mid-winter (January-March), but it competes with an equivalent barotropic ridge aloft, resulting in near-zero surface pressure anomalies. In February, the response resembles the negative phase of the North Atlantic Oscillation, the dominant internal mode of winter circulation variability. In April, the surface trough over the Arctic is accompanied by low pressure anomalies aloft.

Comparison of the CAM3 results with the coupled model response to GHG forcing reveals that Arctic sea ice loss accounts for most of the seasonal, spatial, and vertical structure of the late 21st century high latitude terrestrial air temperature change in CCSM3. Arctic sea ice loss also accounts for much of CCSM3's high latitude SLP response during November-January, but plays a negligible role in the atmospheric circulation response in other months. Finally, Arctic sea ice loss is not the dominant factor in the coupled model's terrestrial snow cover and winter precipitation responses to GHG increases.

5. Discussion

A common criticism of AGCM experiments is that the specified boundary conditions are themselves a response to atmospheric conditions rather than a cause (e.g., Bretherton and Battisti, 2000), and thus the experimental design using a stand-alone

atmospheric model is inappropriate. For the case of future Arctic sea ice loss, however, we have verified that the response of the net surface turbulent (sensible plus latent) energy flux in the region of specified sea ice loss is similar to that in CCSM3, indicating that Arctic sea ice is forcing the atmosphere even in the fully coupled system (not shown).

Our experiments address only the direct impact of Arctic sea ice loss on the atmospheric circulation and climate, and neglect the potential role of oceanic feedbacks. In particular, warming of the Arctic Ocean due to enhanced solar heating associated with sea ice loss may provide additional forcing to the overlying atmosphere, although Singarayer et al. (2006) has shown this effect to be small. In addition, warming of the high latitude north Pacific and Atlantic Oceans due to enhanced downward turbulent energy fluxes as a result of anomalous warm air advection out of the Arctic may also alter the atmospheric circulation response through feedbacks with the midlatitude stormtracks (e.g., Peng et al., 1997; Deser et al., 2007). A follow-up study with an interactive ocean model will be conducted to address the role of oceanic feedbacks.

Magnusdottir et al. (2004) found a consistent negative NAO/NAM-like circulation response in each of the winter months examined (December-March), with the strongest amplitude in March. Their findings are generally consistent with those reported in Seierstad and Bader (2008). In this study, we find different circulation responses in early (November-December) and middle (January-March) winter. The early winter responses are not NAO-like, and exhibit negative SLP values over the Arctic, the Bering Sea and northeastern Canada with a baroclinic structure in the vertical. This early winter response closely resembles that found by Singarayer et al. (2006) for December-February

averages. The middle winter response exhibits negligible SLP change over the Arctic, and a strong negative NAO pattern in February. Further research is needed to understand the reasons for the disparity in the winter circulation responses among different studies.

The lack of a pronounced summertime circulation response found in this study, although consistent with the small net surface energy flux response to the imposed sea ice loss, is at odds with the results of Bhatt et al. (2008). In that study, a statistically significant equivalent barotropic high pressure anomaly over the north Pacific (maximum SLP amplitude ~ 2hPa) was found in response to specified sea ice extent anomalies taken from observations in August 1995. Such a response is opposite to the 1 hPa low pressure anomaly obtained in this study. The sea ice extent anomaly imposed in the study of Bhatt et al. (2008) is confined to the coastal Arctic seas (Laptev, Kara, East Siberian and Beaufort), and thus differs from the Arctic-wide decrease in summer sea ice concentration used in our experiments. Also, sea ice thickness was kept constant at 2m in Bhatt et al. (2008), different from the treatment of sea ice thickness in our study. In summary, it appears prudent to acknowledge that large uncertainties remain in quantifying the dynamical atmospheric response to future Arctic sea ice loss. The thermodynamic response to future Arctic sea ice loss, however, may be more robust than the dynamical response.

With the caveats noted above, the results shown here may serve as a guide to the direct impact of projected future Arctic sea ice loss upon climate and atmospheric circulation. Indeed, the emerging signal of enhanced autumn warming over the Arctic in the past ~ 5 yrs (Serreze et al., 2008) exhibits many similarities with the simulated response to Arctic sea ice loss documented in this study. It remains to be seen whether

other aspects of the simulated response become detectable in the near future as Arctic sea ice continues to decline.

Acknowledgements

We gratefully acknowledge support from the National Science Foundation's Arctic System Science Program. The National Center for Atmospheric Research is sponsored by the National Science Foundation.

References

Alexander, M. A., U. S. Bhatt, J. E. Walsh, M. S. Timlin, J. S. Miller and J. D. Scott, 2004: The atmospheric response to realistic Arctic sea ice anomalies in an AGCM during Winter. *J. Climate* , 17, 890-905.

Bhatt, U. S., M. A. Alexander, C. Deser, J. E. Walsh, J.S. Miller, M. Timlin, J. D. Scott, and R. Tomas, 2008: The Atmospheric Response to Realistic Reduced Summer Arctic Sea Ice Anomalies. In AGU Monograph Arctic Sea Ice Decline: Observations, Projections, Mechanisms, and Implications, E. DeWeaver and C. Bitz., editors.

Bretherton C.S., and D.S. Battisti, 2000: An interpretation of the results from atmospheric general circulation models forced by the time history of the observed sea surface temperature distribution. *Geophys. Res. Lett*., 27, 767-770.

Collins, W.D., C.M. Bitz, M.L. Blackmon, G.B. Bonan, C.S. Bretherton, J.A. Carton, P. Chang, S.C. Doney, J.J. Hack, T.B. Henderson, J.T. Kiehl, W.G. Large, D.S. McKenna, B.D. Santer, and R.D. Smith, 2006: The Community Climate System Model Version 3 (CCSM3). *J. Climate*, 19, 2122-2143.

Comiso, J. C., Parkinson, C.L., Gersten, R., and Stock, L., 2008: Accelerated decline in the Arctic sea ice cover. *Geophys. Res. Lett.*, 35, doi:10.1029/2007GL031972.

Deser, C., J.E. Walsh, and M.S. Timlin, 2000: Arctic sea ice variability in the context of recent atmospheric circulation trends. *J. Climate*, 13, 617-633.

Deser C., G. Magnusdottir, R. Saravanan, and A. S. Phillips, 2004: The effects of North Atlantic SST and sea-ice anomalies on the winter circulation in CCM3. Part II: Direct and indirect components of the response. *J. Climate*, 17, 877-889.

Deser, C. and H. Teng, 2008: Recent Trends in Arctic Sea Ice and the Evolving Role of Atmospheric Circulation Forcing, 1979-2007. In AGU Monograph Arctic Sea Ice Decline: Observations, Projections, Mechanisms, and Implications, E. DeWeaver and C. Bitz., editors.

Gerdes, R., 2006: Atmospheric response to changes in Arctic sea ice thickness. *Geophys. Res. Lett.*, 33(18): L18709.

Hack J. J., J. M. Caron, G. Danabasoglu, K. W. Oleson, C. Bitz, and J. Truesdale, 2006: CCSM-CAM3 climate simulation sensitivity to changes in horizontal resolution. *J. Climate*, 19, 2267-2289.

Hall, N. M. J., J. Derome, and H. Lin, 2001: The extratropical signal generated by a midlatitude SST anomaly. Part I: Sensitivity at equilibrium. *J. Climate*, 14, 2035-2053.

Holland, M. M., C. M. Bitz, and B. Tremblay, 2006: Future abrupt reductions in the summer Arctic sea ice. *Geophys. Res. Lett*., 33, L23503, doi:10.1029/2006GL028024.

Holton, J. R., 1979: An Introduction to Dynamic Meteorology. International Geophysics Series, volume 23, Academic Press, 391 pp.

Honda, M., K. Yamazaki, H. Nakamura, and K. Takeuchi, 1999: Dynamic and thermodynamic characteristics of atmospheric response to anomalous sea–ice extent in the Sea of Okhotsk, *J. Climate*, 12, 3347–33

Hurrell, J. W., 1995: Decadal trends in the North Atlantic Oscillation: Regional temperatures and precipitation. *Science*, 269, 676-679.

Hurrell, J.W., J.J. Hack, A.S. Phillips, J. Caron, and J. Yin, 2006: The Dynamical Simulation of the Community Atmosphere Model Version 3 (CAM3). *J. Climate*, 19, 2162-2183.

Kvamstø, N. G., P. Skeie, and D. B. Stephenson, 2004: Impact of Labrador sea-ice extent on the North Atlantic Oscillation, *Int. J. Climatol*., 24, 603–612.

Lau N.-C., and E. O. Holopainen, 1984: Transient eddy forcing of the time-mean flow as identified by geopotential tendencies. *J. Atmos. Sci*., 41, 313–328.

Lawrence, D.M., A.G. Slater, R.A. Tomas, M.M. Holland, and C. Deser, 2008: Accelerated Arctic land warming and permafrost degradation during rapid sea ice loss. *Geophys. Res. Lett*., 35, L11506, doi:10.1029/2008GL033985.

Magnusdottir G., C. Deser, and R. Saravanan, 2004: The effects of North Atlantic SST and sea-ice anomalies on the winter circulation in CCM3. Part I: Main features and storm-track characteristics of the response. *J. Climate*, 17, 857-876.

Meehl, G.A., W.M. Washington, B.D. Santer, W.D. Collins, J.M. Arblaster, A. Hu, D.M. Lawrence, H. Teng, L.E. Buja, and W.G. Strand, 2006: Climate Change Projections for the Twenty-First Century and Climate Change Commitment in the CCSM3. *J. Climate*, 19, 2597–2616.

Peng, S.L., W. A. Robinson, and M. P. Hoerling, 1997: The modeled atmospheric response to midlatitude SST anomalies and its dependence on background circulation states. *J. Climate*, 10, 971-987.

Post, E. and M. C. Forchhammer, 2008: Climate change reduces reproductive success of an Arctic herbivore through trophic mismatch. *J. Phil. Trans. Roy. Soc. B*, 363, doi10.1098/rstb.2007.2207.

Seierstad, I. A., and J. Bader, 2008: Impact of a projected future Arctic sea ice reduction on extratropical storminess and the NAO, *Clim. Dyn*. doi10.1007/s00382-008-0463-x, in press.

Serreze, M. C., M. M. Holland, and J. Stroeve, 2007: Perspectives on the Arctic's shrinking sea-ice cover. *Science*, 315, 1533-1536.

Serreze, M. C., A.P. Barrett, J.C. Stroeve, D.N. Kindig, and M.M. Holland, 2008: The emergence of surface-based Arctic amplification, *The Cryosphere Discuss*., 2, 601-622.

Sewall, J.O., 2005: Precipitation shifts over western North America as a result of declining Arctic sea ice cover, the coupled system response. *Earth Interactions*, 9, 1-23.

Singarayer, J.S., J.L. Bamber and P.J. Valdes, 2006: Twenty-first-Century climate impacts from a declining Arctic sea ice cover. J. Climate, 19, 1109-1125.

Stroeve, J., M. M. Holland, W. Meier, T. Scambos, and M. C. Serreze, 2007: Arctic sea ice decline: faster than forecast. *Geophys. Res. Lett*., 34, doi:10.1029/2007GL029703.

Ting M., and S. Peng, 1995: Dynamics of the early and middle winter atmospheric responses to northwest Atlantic SST anomalies. *J. Climate*, 8, 2239-2254.

Wallace J. M., 2000: North Atlantic Oscillation/annular mode: Two paradigms—One phenomenon. *Quart. J. Roy. Meteor. Soc*, 126, 791–80.

Figure Captions

Figure 1. Bi-monthly distributions of Arctic a) sea ice concentration (%) and b) sea ice thickness (m) during 1980-1999 and 2080-2099 from CCSM3.

Figure 2. (Top two rows) Bi-monthly Arctic sea ice thickness (ΔSIT; m) and concentration (ΔSIC; %) differences (2080-2099 minus 1980-1999) from CCSM3. (Bottom 3 rows) Bi-monthly turbulent energy flux (ΔSH+LH), longwave radiative flux (ΔLW) and shortwave radiative flux (ΔSW) responses to sea ice cover changes. Fluxes are given in units of Wm^{-2} and are positive upward.

Figure 3. Seasonal cycle of the turbulent energy flux (ΔSH+LH; thin solid curve), longwave radiative flux (ΔLW; dotted curve) and shortwave radiative flux (ΔSW; dashed curve) responses area-averaged over the Arctic Ocean. The net surface energy flux response is given by the thick solid curve, and the SIC changes (%) are indicated by the gray bars (note the inverted scale). Fluxes are given in units of Wm^{-2} (positive upward).

Figure 4. Seasonal cycles of air temperature (ºC; dotted curve) and precipitation (mm d^{-1}; dashed curve) area-averaged over a) the Arctic Ocean, and b) the high latitude continents (65º - 80ºN; 60 º -300 º E). The solid curve in both panels shows the sum of the turbulent and longwave fluxes area-averaged over the Arctic Ocean (Wm^{-2}). SIC changes are indicated by the gray bars (scale as in Fig. 3, not shown).

Figure 5. Bi-monthly responses of net surface energy flux (ΔQnet; Wm^{-2}), terrestrial air temperature (ΔAir T; ºC), terrestrial snow depth (ΔSnow; cm liquid water equivalent) and terrestrial precipitation (ΔPrecip; mm d^{-1}). Color scales are given at the bottom of the figure. Thick black contours on the air temperature panels outline regions with a low-level temperature inversion ($T_{850hPa} - T_{1000hPa} > 0$ ºC) during 1980-1999. Precipitation responses significant at the 5% confidence level are outlined with black contours.

Figure 6. Vertical profiles of atmospheric temperature during 1980-1999 (dashed curves) and 2080-2099 (solid curves) over the Arctic Ocean (left panel) and high latitude (65º - 80ºN) continents (middle panel) in December. (Right panel) 2080-99 minus 1980-99 differences over the Arctic Ocean (thick curve) and high latitude continents (thin curve).

Figure 7. Geographical distributions of the strength of the December low-level inversion ($T_{850hPa} - T_{1000hPa} > 0$ ºC) during 1980-1999 (left) and 2080-99 (right). Values < 1.5 ºC not shown.

Figure 8. Seasonal cycles of $T_{850hPa} - T_{1000hPa}$ during 1980-1999 (dark gray) and 2080-2099 (light gray) over the Arctic Ocean (top) and high latitude continents (middle). The bottom panel shows the 2080-99 minus 1980-99 differences for the Arctic Ocean (light gray) and high latitude continents (dark gray).

Figure 9. Accumulated cold season (October – March) precipitation and March snow depth responses (cm). The thick black and gray contours on the snow panel denote the -10 ºC and 0 ºC air temperature isotherms, respectively, during 2080-2099.

Figure 10. Seasonal cycles of precipitation (mm d^{-1}; dashed curve), accumulated precipitation (cm; dotted curve), and snow depth (cm liquid water equivalent; solid curve) responses for a) northern Canada and b) Siberia.

Figure 11. Heat budget response (ºC per day) for the Arctic Ocean (left) and high latitude (65º-80ºN) continents (right). Sub-monthly transient temperature advection (solid black curve); monthly mean temperature advection (dashed black curve); condensational heating (dashed purple curve); vertical and horizontal diffusion (green curve); longwave radiation (solid purple curve). The time-tendency and shortwave radiation terms are negligible (not shown). The sum of all the terms (e.g., the heat budget residual) is given by the orange curve.

Figure 12. Monthly geopotential height responses at 1000 hPa and 500 hPa. The contour interval is 10m, with positive (negative) values in red (blue) and the zero contours omitted. Shading indicates values that exceed the 5% confidence level based on a two-sided Student's t-test.

Figure 13. Vertical structures of the geopotential height (m; contours) and temperature (ºC; color shading) responses along 90º E in November-December, January-February, and April.

Figure 14. a) Bi-monthly terrestrial air temperature responses (ºC) for CCSM3 (top) and CCSM3 minus CAM3 (bottom). b) Seasonal cycle of the high latitude (65º - 80ºN) terrestrial air temperature response in CCSM3 (dashed), CAM3 (solid), and their difference (dotted). c) Vertical profiles of the December high latitude (65º - 80ºN) terrestrial air temperature response in CCSM3 (dashed), CAM3 (solid), and their difference (dotted).

Figure 15. Accumulated cold season (October – March) precipitation and March snow depth responses (cm) in CCSM3. The thick black and gray contours on the snow panel denote the -10 ºC and 0 ºC air temperature isotherms, respectively, during 2080-2099.

Figure 16. Monthly SLP responses for CAM3 and CCSM3. The contour interval is 1hPa, with positive (negative) values in red (blue) and the zero contours omitted. Shading indicates values that exceed the 5% confidence level based on a two-sided Student's t-test.

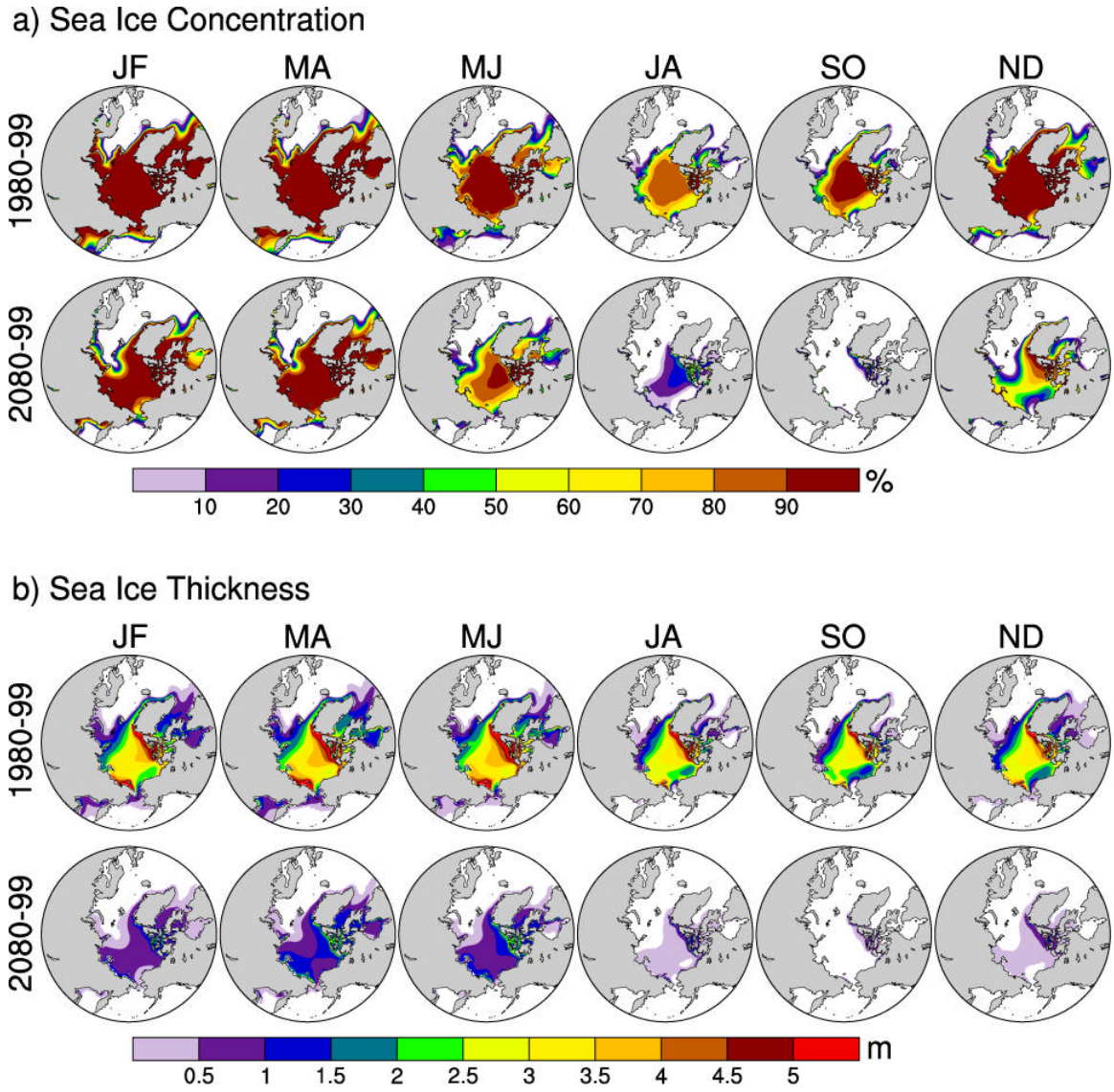

Figure 1. Bi-monthly distributions of Arctic a) sea ice concentration (%) and b) sea ice thickness (m) during 1980-1999 and 2080-2099 from CCSM3.

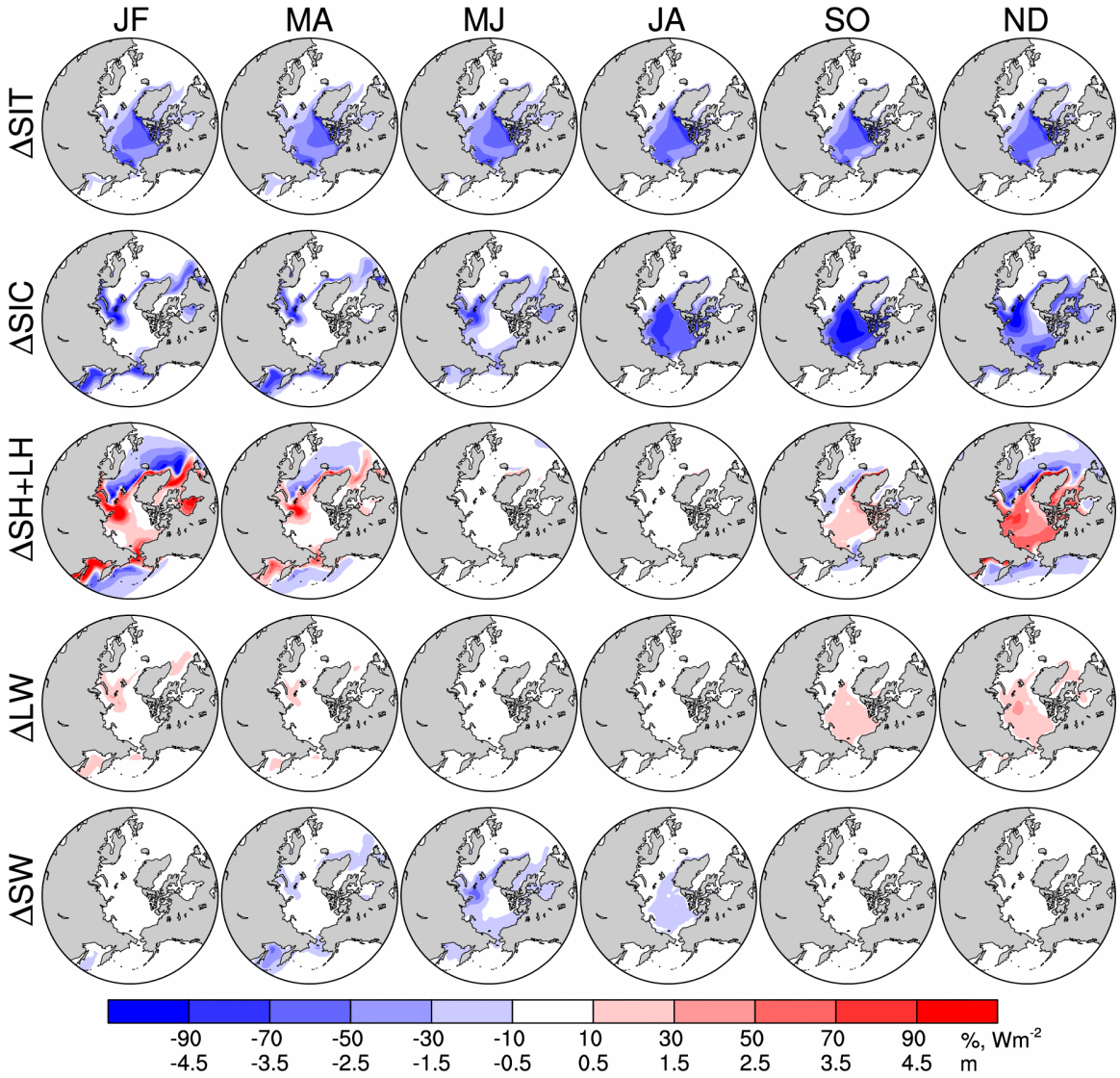

Figure 2. (Top two rows) Bi-monthly Arctic sea ice thickness (ΔSIT; m) and concentration (ΔSIC; %) differences (2080-2099 minus 1980-1999) from CCSM3. (Bottom 3 rows) Bi-monthly turbulent energy flux (ΔSH+LH), longwave radiative flux (ΔLW) and shortwave radiative flux (ΔSW) responses to sea ice cover changes. Fluxes are given in units of Wm^{-2} and are positive upward.

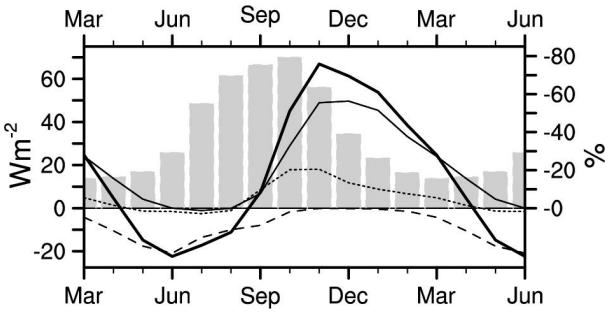

Figure 3. Seasonal cycle of the turbulent energy flux (ΔSH+LH; thin solid curve), longwave radiative flux (ΔLW; dotted curve) and shortwave radiative flux (ΔSW; dashed curve) responses area-averaged over the Arctic Ocean. The net surface energy flux response is given by the thick solid curve, and the SIC changes (%) are indicated by the gray bars (note the inverted scale). Fluxes are given in units of Wm^{-2} (positive upward).

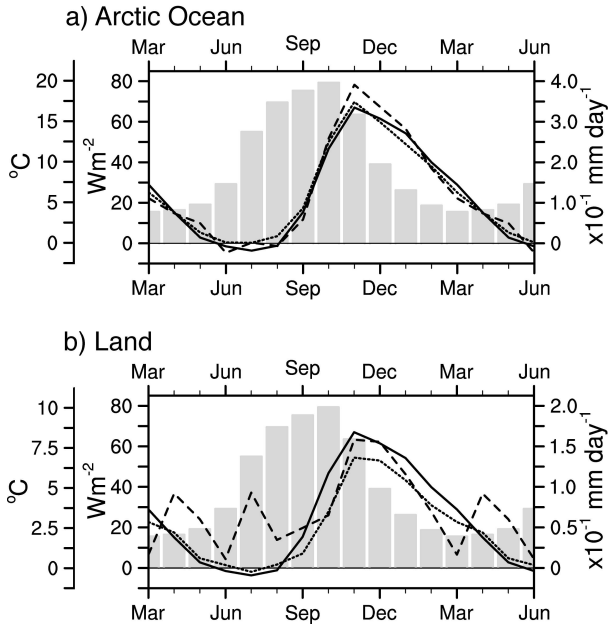

Figure 4. Seasonal cycles of air temperature (ºC; dotted curve) and precipitation (mm d^{-1}; dashed curve) area-averaged over a) the Arctic Ocean, and b) the high latitude continents (65º - 80ºN; 60 º -300 º E). The solid curve in both panels shows the sum of the turbulent and longwave fluxes area-averaged over the Arctic Ocean (Wm^{-2}). SIC changes are indicated by the gray bars (scale as in Fig. 3, not shown).

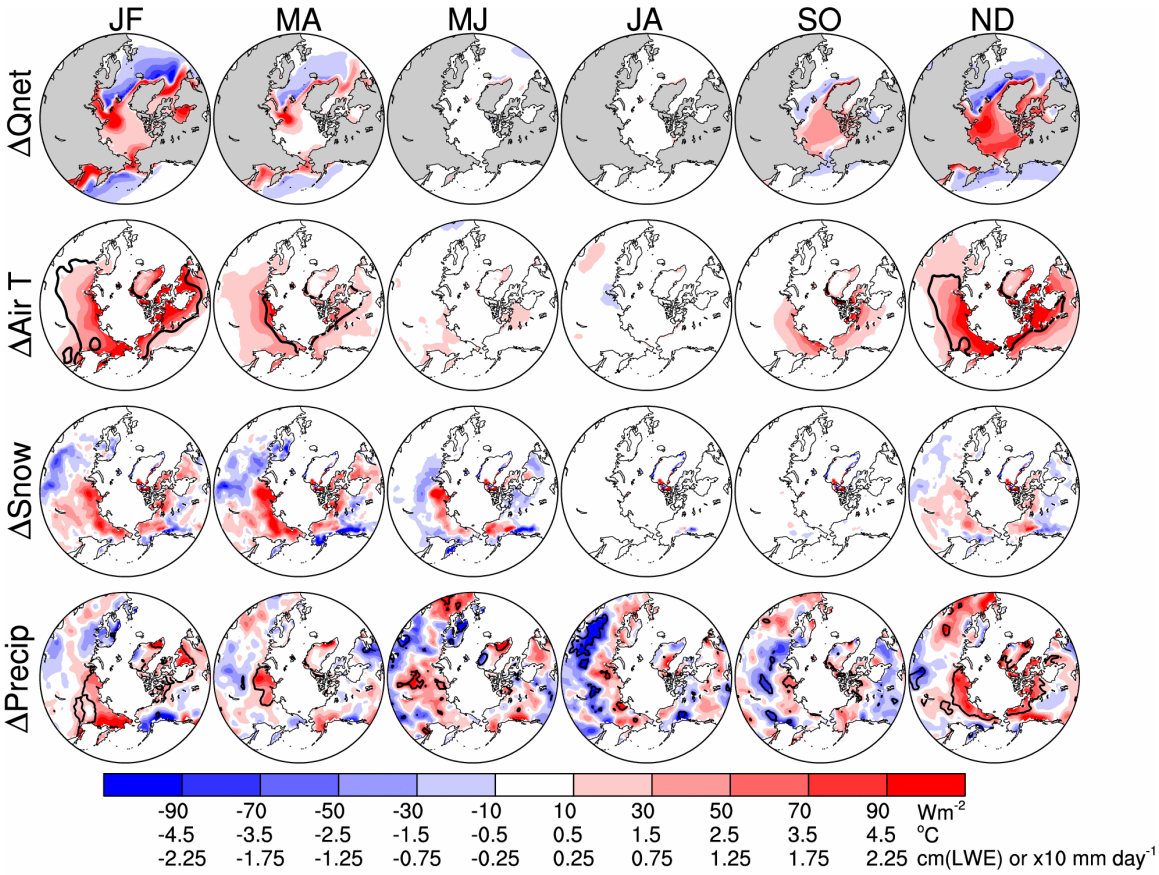

Figure 5. Bi-monthly responses of net surface energy flux (ΔQnet; Wm^{-2}), terrestrial air temperature (ΔAir T; ºC), terrestrial snow depth (ΔSnow; cm liquid water equivalent) and terrestrial precipitation (ΔPrecip; mm d^{-1}). Color scales are given at the bottom of the figure. Thick black contours on the air temperature panels outline regions with a low-level temperature inversion ($T_{850hPa} - T_{1000hPa} > 0$ ºC) during 1980-1999. Precipitation responses significant at the 5% confidence level are outlined with black contours.

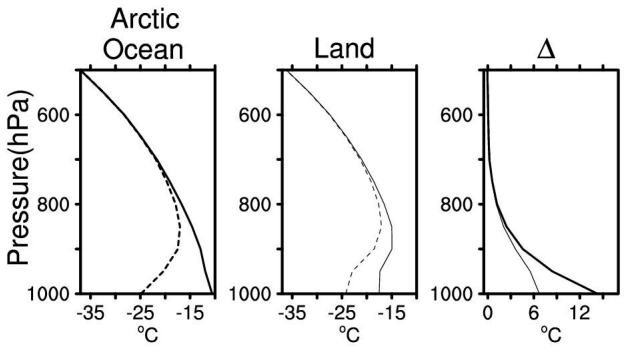

Figure 6. Vertical profiles of atmospheric temperature during 1980-1999 (dashed curves) and 2080-2099 (solid curves) over the Arctic Ocean (left panel) and high latitude (65º - 80ºN) continents (middle panel) in December. (Right panel) 2080-99 minus 1980-99 differences over the Arctic Ocean (thick curve) and high latitude continents (thin curve).

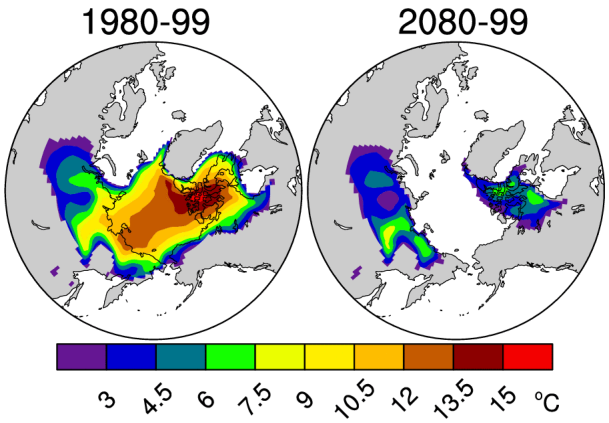

Figure 7. Geographical distributions of the strength of the December low-level inversion ($T_{850hPa} - T_{1000hPa} > 0$ ºC) during 1980-1999 (left) and 2080-99 (right). Values < 1.5 ºC not shown.

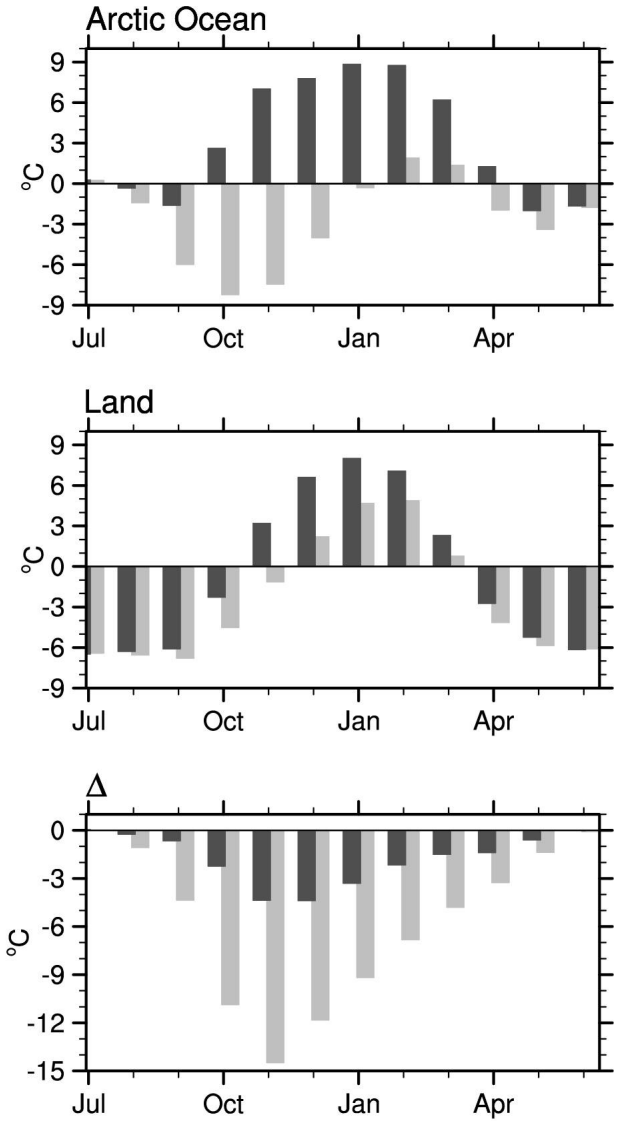

Figure 8. Seasonal cycles of $T_{850hPa} - T_{1000hPa}$ during 1980-1999 (dark gray) and 2080-2099 (light gray) over the Arctic Ocean (top) and high latitude continents (middle). The bottom panel shows the 2080-99 minus 1980-99 differences for the Arctic Ocean (light gray) and high latitude continents (dark gray).

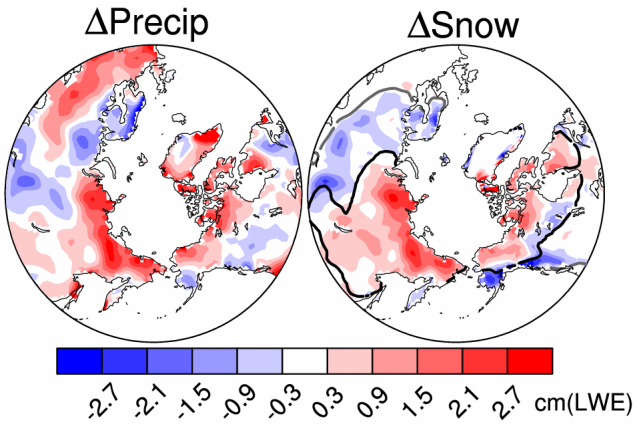

Figure 9. Accumulated cold season (October – March) precipitation and March snow depth responses (cm). The thick black and gray contours on the snow panel denote the -10 ºC and 0 ºC air temperature isotherms, respectively, during 2080-2099.

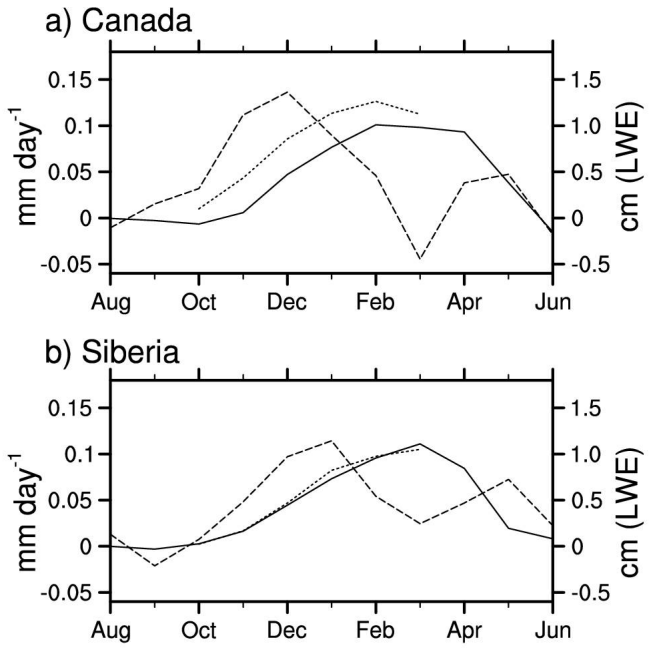

Figure 10. Seasonal cycles of precipitation (mm d^{-1}; dashed curve), accumulated precipitation (cm; dotted curve), and snow depth (cm liquid water equivalent; solid curve) responses for a) northern Canada and b) Siberia.

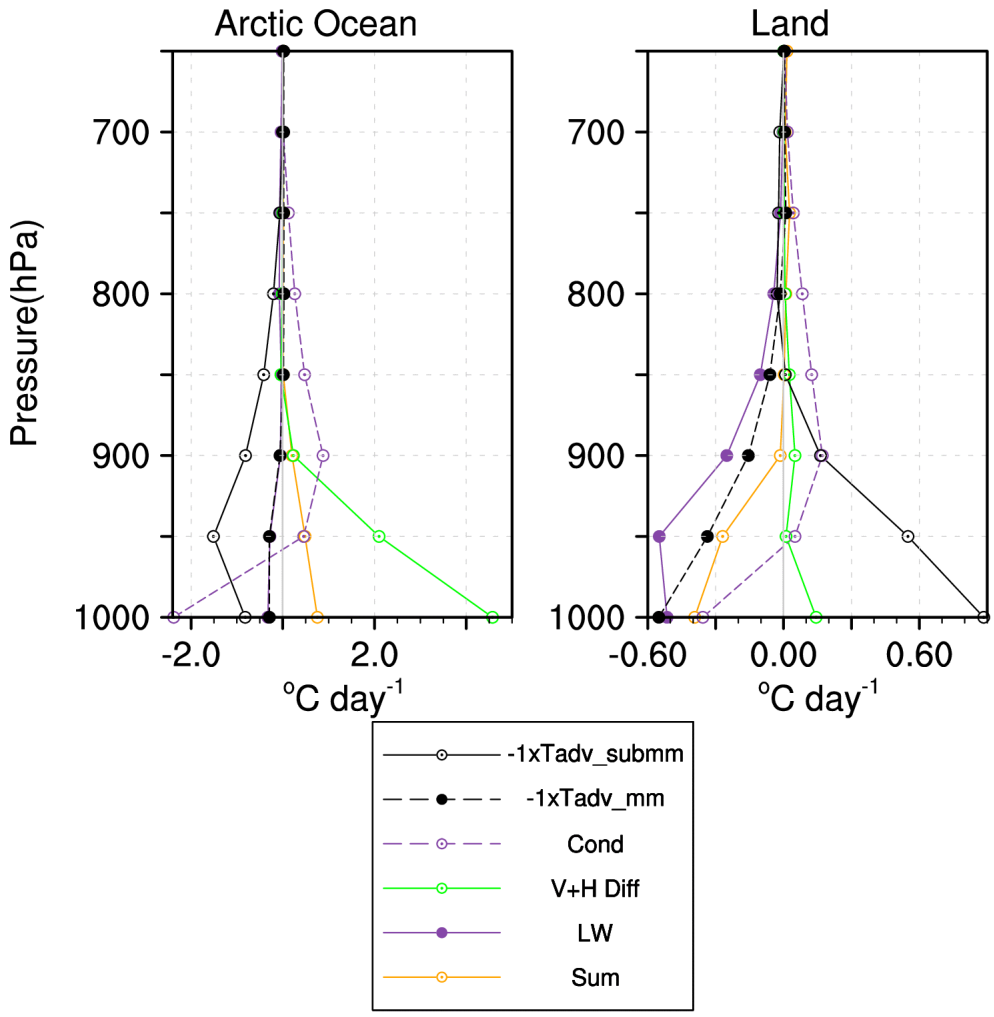

Figure 11. Heat budget response (ºC per day) for the Arctic Ocean (left) and high latitude (65º-80ºN) continents (right). Sub-monthly transient temperature advection (solid black curve); monthly mean temperature advection (dashed black curve); condensational heating (dashed purple curve); vertical and horizontal diffusion (green curve); longwave radiation (solid purple curve). The time-tendency and shortwave radiation terms are negligible (not shown). The sum of all the terms (e.g., the heat budget residual) is given by the orange curve.

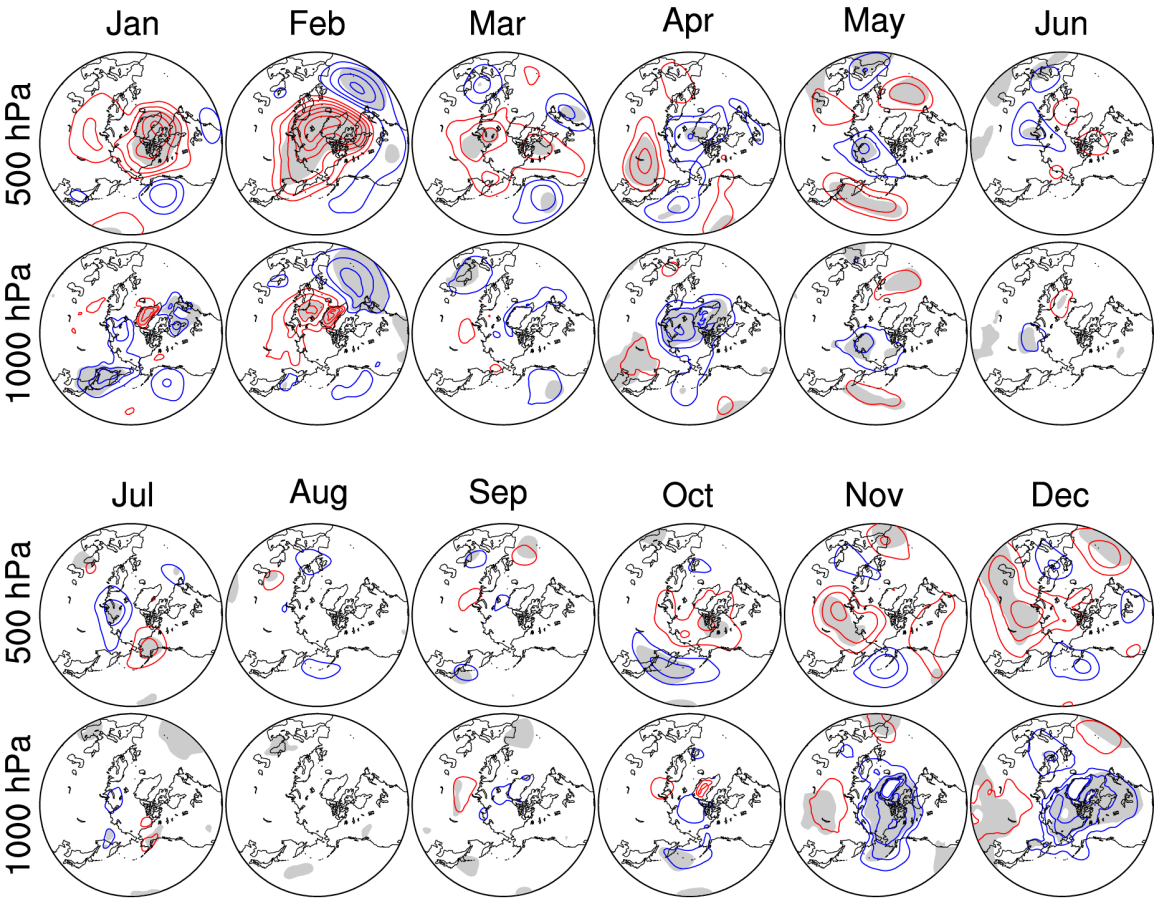

Figure 12. Monthly geopotential height responses at 1000 hPa and 500 hPa. The contour interval is 10m, with positive (negative) values in red (blue) and the zero contours omitted. Shading indicates values that exceed the 5% confidence level based on a two-sided Student's t-test.

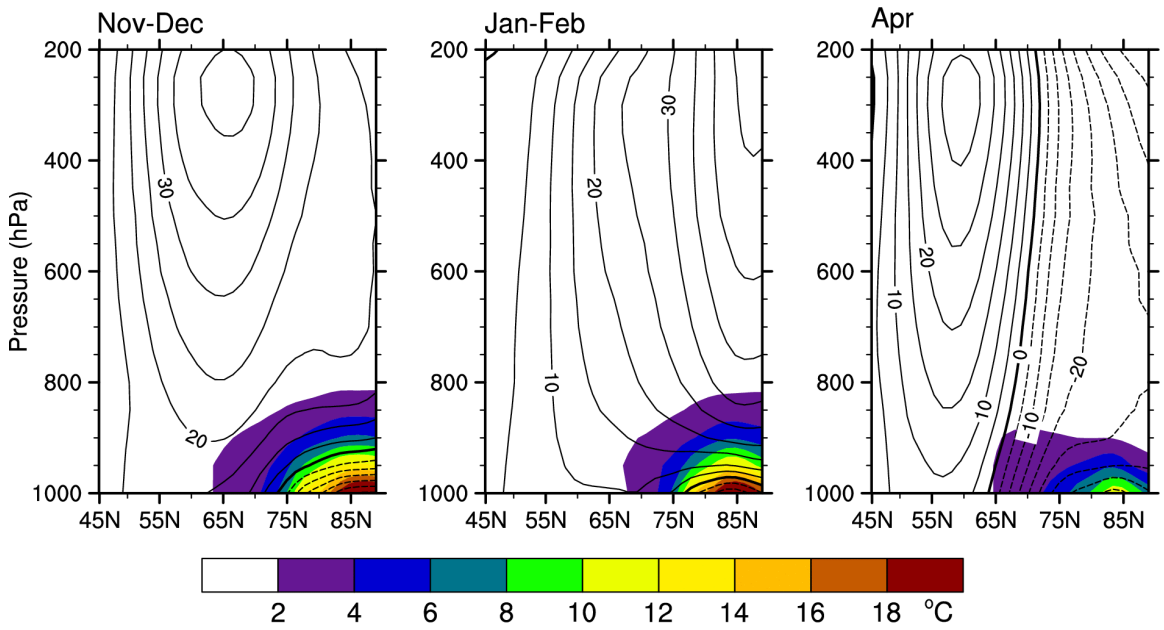

Figure 13. Vertical structures of the geopotential height (m; contours) and temperature (ºC; color shading) responses along 90º E in November-December, January-February, and April.

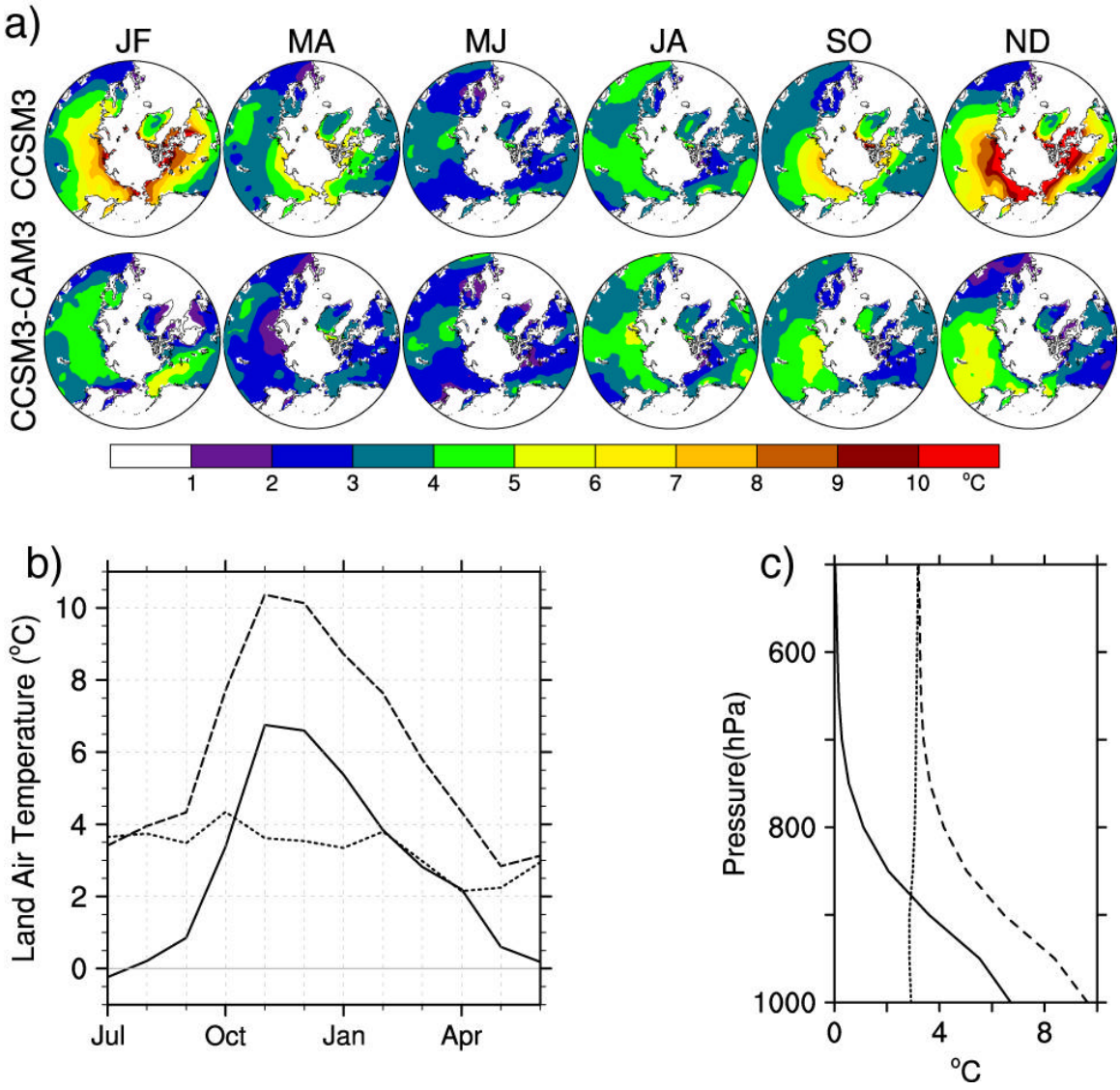

Figure 14. a) Bi-monthly terrestrial air temperature responses (ºC) for CCSM3 (top) and CCSM3 minus CAM3 (bottom). b) Seasonal cycle of the high latitude (65º - 80ºN) terrestrial air temperature response in CCSM3 (dashed), CAM3 (solid), and their difference (dotted). c) Vertical profiles of the December high latitude (65º - 80ºN) terrestrial air temperature response in CCSM3 (dashed), CAM3 (solid), and their difference (dotted).

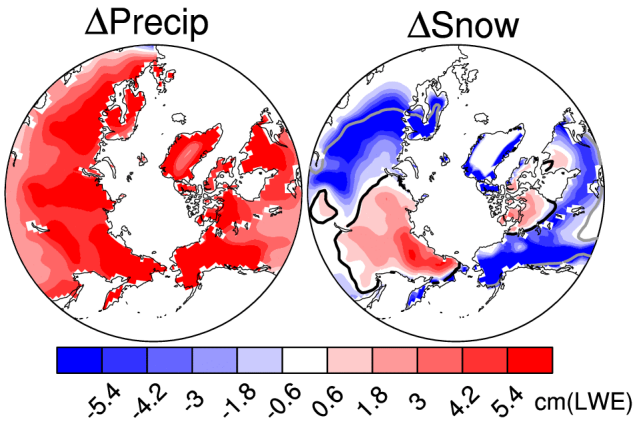

Figure 15. Accumulated cold season (October – March) precipitation and March snow depth responses (cm) in CCSM3. The thick black and gray contours on the snow panel denote the -10 ºC and 0 ºC air temperature isotherms, respectively, during 2080-2099.

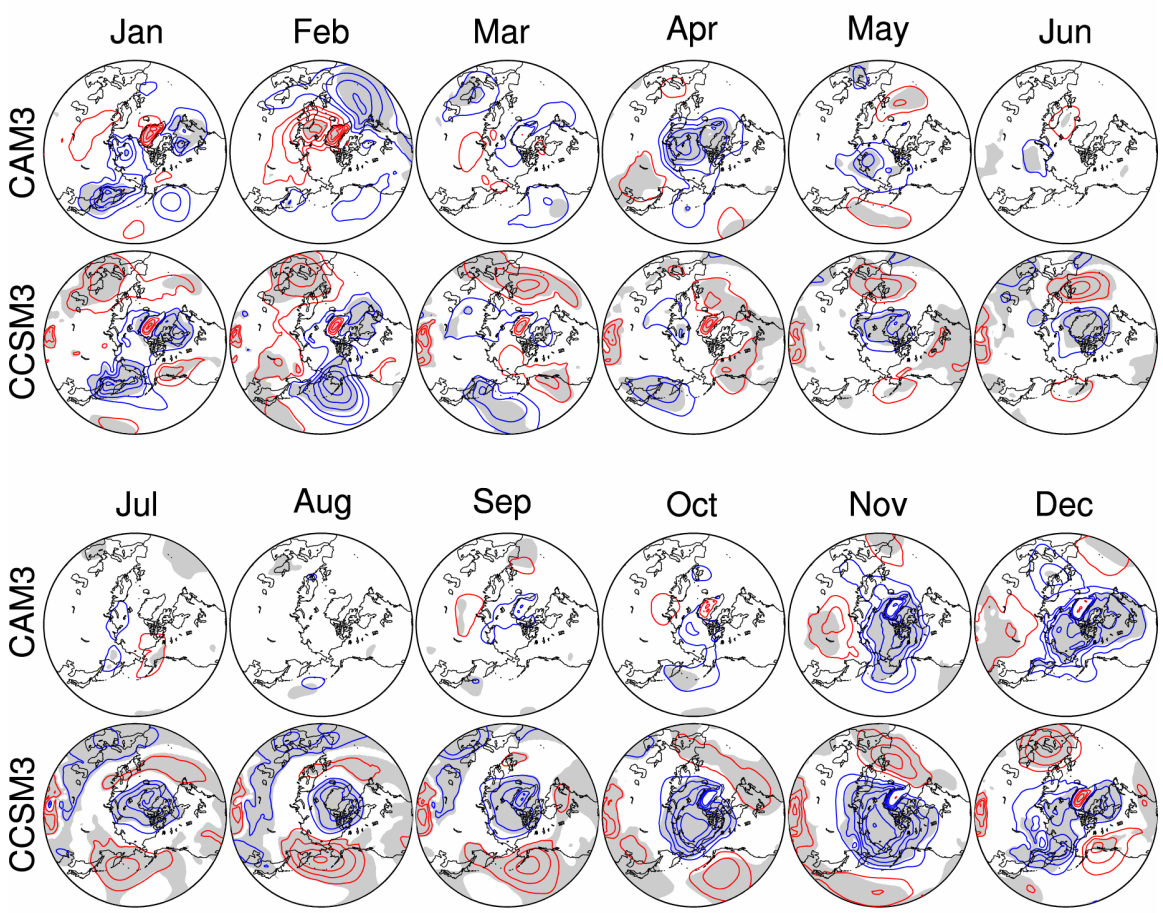

Figure 16. Monthly SLP responses for CAM3 and CCSM3. The contour interval is 1hPa, with positive (negative) values in red (blue) and the zero contours omitted. Shading indicates values that exceed the 5% confidence level based on a two-sided Student's t-test.